ACS APPLIED MATERIALS & INTERFACES

Research Article

www.acsami.org

Iron Telluride-Decorated Reduced Graphene Oxide Hybrid Microspheres as Anode Materials with Improved Na-Ion Storage Properties

Jung Sang Cho,[†] Seung Yeon Lee,[†] Jung-Kul Lee,[*,‡] and Yun Chan Kang[*,†]

[†]Department of Materials Science and Engineering, Korea University, Anam-Dong, Seongbuk-Gu, Seoul 136-713, Republic of Korea

[‡]Department of Chemical Engineering, Konkuk University, 1 Hwayang-dong, Gwangjin-gu, Seoul 143-701, Republic of Korea

Supporting Information

ABSTRACT: Transition-metal telluride materials are studied as the anode materials for Na-ion batteries (NIBs). The $FeTe_2$–reduced graphene oxide (rGO) hybrid powders (first target material) are prepared via spray pyrolysis and subsequent tellurization. The H_2Te gas treatment transforms the Fe_3O_4–rGO powders to $FeTe_2$–rGO hybrid powders with $FeTe_2$ nanocrystals (various sizes <100 nm) embedded within the rGO. The $FeTe_2$–rGO hybrid powders contain 5 wt % rGO. The Na-ion storage mechanism for $FeTe_2$ in NIBs is described by $FeTe_2 + 4Na^+ + 4e^- \leftrightarrow Fe + 2Na_2Te$. The $FeTe_2$–rGO hybrid discharge process forms metallic Fe nanocrystals and Na_2Te by a conversion reaction of $FeTe_2$ with Na ions. The discharge capacities of the $FeTe_2$–rGO hybrid powders for the first and 80th cycles are 493 and 293 mA h g^{-1}, respectively. The discharge capacities of the bare $FeTe_2$ powders for the first and 80th cycles are 462 and 83 mA h g^{-1}, respectively. The $FeTe_2$–rGO hybrid powders have superior Na-ion storage properties compared to bare $FeTe_2$ powders owing to their high structural stability and electrical conductivity.

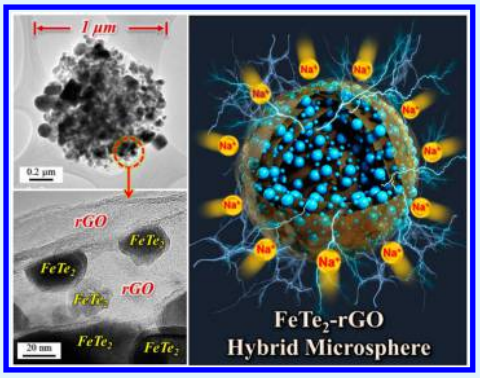

KEYWORDS: *iron telluride, sodium ion batteries, graphene, carbon hybrid, spray pyrolysis*

INTRODUCTION

Na-ion batteries (NIBs) have received significant attention as a feasible alternative for energy storage due to the lower cost of NIBs than Li-ion batteries and the higher natural abundance of Na than Li.[1−5] However, the larger Na^+ ionic radius (1.02 Å for Na^+ vs 0.76 Å for Li^+) and molar mass (22.99 g mol^{-1} for Na vs 6.94 g mol^{-1} for Li) leads to slow sodium ion diffusion kinetics, high structural damage during cycling, and strong coordination in the host lattices.[6−9] These results create critical obstacles for NIBs, such as a low specific capacity, low rate capability, and a short cycling life.

The issues related to the composition of the host materials in NIBs and their hybridization with carbon materials have been studied to overcome these potential problems.[2,3,9−11] Transition-metal chalcogenide materials have been also studied for NIBs.[12−17] Among the transition-metal chalcogenide materials, iron chalcogenide (Fe_xY; Y = S and Se) has attracted considerable attention because of the abundant reserves of Fe and its wide range of compositions and phases.[17−25] Kim et al. employed natural pyrite (FeS_2, Chile) in NIBs; it showed a high discharge capacity of 630 mA h g^{-1} at 50 mA g^{-1}, but the capacity decreased continuously to 85 mA h g^{-1} after 50 cycles.[21] Zhang et al. demonstrated the use of $FeSe_2$ as an anode material for NIBs by preparing $FeSe_2$ microspheres assembled by nanooctahedra via a simple hydrothermal method.[17] $FeSe_2$ microspheres exhibited long-term cyclic stability and an excellent high-rate performance.[17] Park et al. prepared $FeSe_x$–reduced graphene oxide (rGO) composite powders exhibiting high capacities by applying a nanoscale Kirkendall diffusion process.[25] However, to the best of our knowledge, transition-metal telluride materials, including iron telluride ($FeTe_2$), have not been studied as materials for NIBs.

The heavy $FeTe_2$ compound could have less change in volume during the cycling and a high volumetric capacity due to its high density (8.06 g cm^{-3}).[26−28] An ideal battery would have a high density, small volume, and long cycling life. It would also be low-cost and environmentally friendly. Tellurium is an element that is chemically related to selenium and sulfur. Therefore, it is worth confirming the possibility of the application of $FeTe_2$ as an anode material in NIBs.

Transition-metal telluride materials were studied for the first time as a possible candidate for the anode material of NIBs. rGO is considered as the efficient support for transition-metal compounds.[29−33] Herein, $FeTe_2$–rGO hybrid powders selected as the first target material were prepared by a spray pyrolysis process and subsequent tellurization treatment. The Na-ion storage performances of the $FeTe_2$–rGO hybrid powders for Na-ion storage were compared with those of the bare $FeTe_2$ powders.

Received: May 14, 2016
Accepted: August 4, 2016
Published: August 4, 2016

DOI: 10.1021/acsami.6b05758
ACS Appl. Mater. Interfaces 2016, 8, 21343−21349

EXPERIMENTAL SECTION

The $FeTe_2$–rGO hybrid and bare $FeTe_2$ powders were prepared by a two-step process. The one-step tellurization process of the Fe_3O_4–rGO hybrid and bare Fe_2O_3 powders produced the $FeTe_2$–rGO hybrid and bare $FeTe_2$ powders, respectively. The Fe_3O_4–rGO powders were prepared by spray pyrolysis from the iron nitrate nonahydrate ($Fe(NO_3)_3{\cdot}9H_2O$, Sigma-Aldrich, 98%) spray solution with graphene oxide (GO) nanosheets (Figure S1). The formation procedure of colloidal GO solution was described in our previous reports.[34,35] In the spray pyrolysis process, the reactor temperature and flow rate of the Ar gas were 600 °C and 8 L min^{-1}, respectively. After the spray pyrolysis process, a tellurization process was performed at 400 °C for 12 h under a 10% H_2/Ar gas with tellurium metal powders (Te; Sigma-Aldrich, 99.8%). The precursor powders for the bare Fe_2O_3 powders were prepared by a spray drying process from the spray solution of iron nitrate nonahydrate and sucrose ($C_{12}H_{22}O_{11}$, Junsei; shown in Figure S2). The Fe_2O_3 powders without carbon were produced by post-treatment of the spray-dried powders at 500 °C under an air atmosphere. The tellurization process of the Fe_2O_3 powders at 450 °C produced the bare $FeTe_2$ powders. Detailed characterization method and electrochemical measurements procedure are described in the Supporting Information.

RESULTS AND DISCUSSION

The formation scheme of the $FeTe_2$–rGO hybrid powder is shown in Figure 1. The Fe_3O_4–rGO hybrid precursor powder

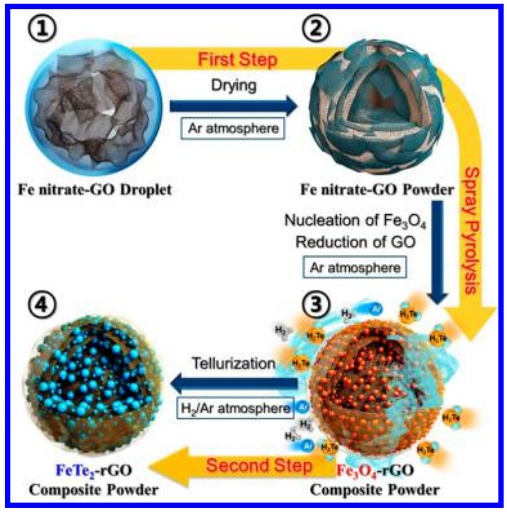

Figure 1. Formation scheme of the $FeTe_2$-decorated rGO hybrid powders formed by tellurization of Fe_3O_4-decorated rGO hybrid powders: ① Fe nitrate–GO droplet, ② Fe nitrate–GO powder, ③ Fe_3O_4–rGO composite powder, and ④ $FeTe_2$–rGO composite powder.

was prepared by spray pyrolysis process from a colloidal solution of iron nitrate and GO nanosheets (Figure 1①–③). GO nanosheets minimized the phase segregation of iron nitrate during the droplet drying process (Figure 1②). In addition, rGO nanosheets formed by the thermal reduction of GO nanosheets minimized the growth of the Fe_3O_4 nanocrystals (formed by decomposition of iron nitrate under an Ar atmosphere; see Figure 1③). Therefore, Fe_3O_4 nanocrystals were well-distributed within the crumpled rGO matrix in the Fe_3O_4–rGO hybrid powder (Figure 1③). The one-step post-treatment under H_2Te gas (formed from Te powder via a reaction with H_2 gas, Te (s) + H_2 (g)→H_2Te (g)) transformed the Fe_3O_4–rGO into the $FeTe_2$–rGO hybrid powder with a similar morphology by Fe_3O_4 (s) + $6H_2Te$ (g) → $3FeTe_2$ (s) + $4H_2O$ (g) + $2H_2$ (g) (Figure 1④).

The characteristics of the precursor Fe_3O_4–rGO hybrid powder prepared by a spray pyrolysis at 600 °C are shown in Figure S3. The hybrid powders had a crumpled structure and there was minimal aggregation between the powders (Figure S3a). The ultrafine Fe_3O_4 nanocrystals with the mean size of 4 nm are uniformly embedded within the rGO matrix as shown by transmission electron microscopy (TEM) images. The high-resolution (HR) TEM image shown in Figure S3e showed clear lattice fringes separated by 0.25 nm corresponding to the (113) crystal plane of Fe_3O_4. The Ar atmosphere in the spray pyrolysis process formed oxygen-deficient Fe_3O_4 nanocrystals, as confirmed by XRD pattern in Figure S3b. The morphology of the $FeTe_2$–rGO hybrid powder formed by the tellurization process of the Fe_3O_4–rGO precursor powder is shown in Figure 2. The scanning electron microscopy (SEM) image

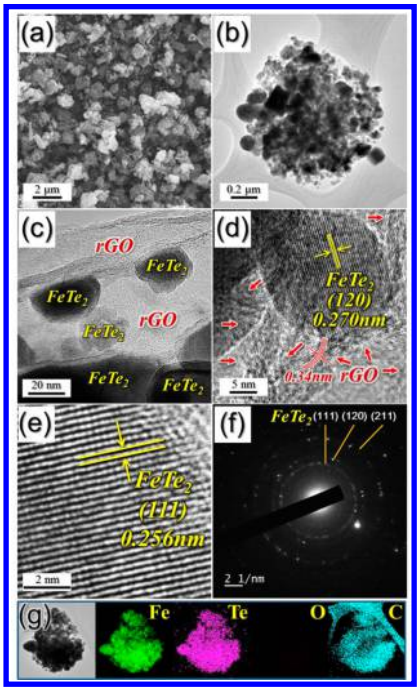

Figure 2. Morphologies, SAED pattern, and elemental mapping images of the $FeTe_2$-decorated rGO hybrid powders: (a) SEM image, (b, c) TEM images, (d, e) HR-TEM images, (f) SAED pattern, and (g) elemental mapping images.

shown in Figure 2a revealed the spherical shape and crumpled structure of the nonaggregated $FeTe_2$–rGO hybrid powders (mean size of 1.0 μm). The $FeTe_2$ nanocrystals (various sizes <100 nm) were uniformly embedded within the rGO matrix, as shown by the TEM images in Figure 2b,c. The ultrafine Fe_3O_4 nanocrystals embedded within the Fe_3O_4–rGO hybrid powder transformed into the $FeTe_2$ crystals with various sizes during the 12 h tellurization process at 400 °C. The HR-TEM images shown in Figure 2d,e showed clear lattice fringes of the (120) and (111) crystal planes for orthorhombic $FeTe_2$ and (001) crystal plane of the rGO phase. The selected area electron diffraction (SAED) and X-ray diffraction (XRD) patterns shown in Figure 2f and Figure 3a, respectively, confirmed the formation of the $FeTe_2$–rGO hybrid powder with a pure $FeTe_2$ crystal structure. The elemental mapping images shown in

DOI: 10.1021/acsami.6b05758
ACS Appl. Mater. Interfaces 2016, 8, 21343–21349

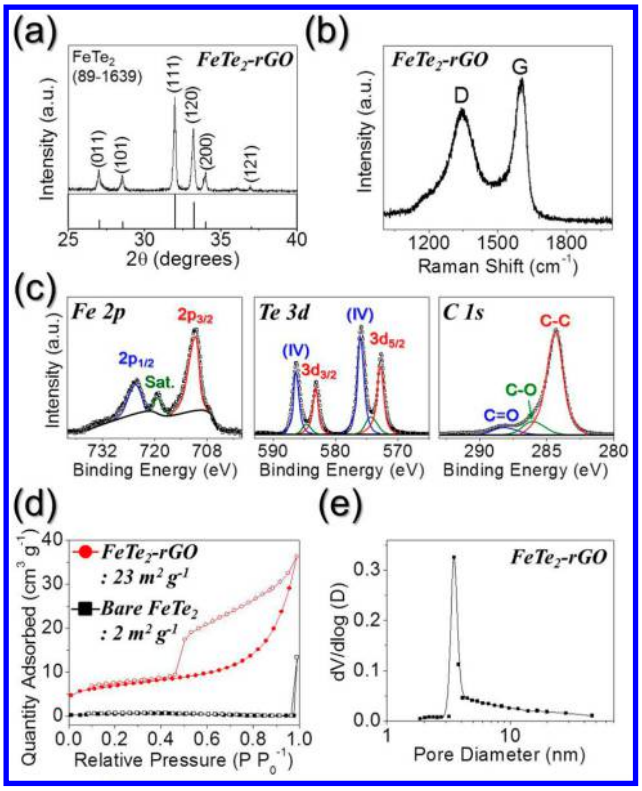

Figure 3. (a) XRD pattern, (b) Raman spectrum, and (c) XPS spectra of the $FeTe_2$-decorated rGO hybrid powders. (d) N_2 adsorption and desorption isotherms of the $FeTe_2$-decorated rGO hybrid powders and bare $FeTe_2$ powders. (e) BJH adsorption pore size distribution of the $FeTe_2$-decorated rGO hybrid powders.

Figure 2g revealed the uniform distribution of the $FeTe_2$ nanocrystals on the $FeTe_2$−rGO hybrid powder.

The Raman spectrum of the $FeTe_2$−rGO hybrid powder (Figure 3b) exhibited two characteristic main peaks of graphene: the D band at 1340 cm^{-1} and the G band at 1580 cm^{-1}.[36] The ratio of the peak intensity between the D and G bands of the $FeTe_2$−rGO hybrid powder was ~0.91, indicating that defects or edge areas of the rGO formed during the spray pyrolysis and long-term tellurization processes. The X-ray photoelectron spectroscopy (XPS) spectra of the $FeTe_2$−rGO hybrid powders are shown in Figure 3c. The main peaks of the $FeTe_2$−rGO hybrid powder (Fe 2p spectrum) occurred at binding energies of 711 eV for Fe $2p_{3/2}$ and 724 eV for Fe $2p_{1/2}$; these are characteristic of $FeTe_2$ phase.[37] In the Te 3d spectrum, the peaks at 572.6 and 582.9 eV correspond to Te $3d_{5/2}$ and Te $3d_{3/2}$, respectively, which originate from the $FeTe_2$ phase.[37] Along with these, two peaks were additionally observed at 576.0 and 586.3 eV attributed to Te(IV) oxide due to the long exposure of the powders to an air atmosphere.[37] The C 1s spectrum revealed peaks corresponding to C−C, C−O, and C═O bonds at 284.2, 286.4, and 288.1 eV, respectively.[38] The strong C−C bond peak indicated the thermal reduction of the GO nanosheets to rGO nanosheets during the preparation process. The N_2 adsorption and desorption isotherms of the $FeTe_2$−rGO hybrid powders (Figure 3d) had a clear hysteresis loop that resembled the type-H1 isotherm classification.[39] This revealed the presence of mesopores within the $FeTe_2$−rGO hybrid powders. The Barrett−Joyner−Halenda (BJH) pore size distribution derived from the adsorption branch of the isotherm confirmed the well-developed mesopores in the $FeTe_2$−rGO hybrid powders with a pore size of ~3.5 nm (Figure 3e). The thermogravimetric (TG) curve of the $FeTe_2$−rGO hybrid powders (Figure S4) revealed a gradual weight increase at temperatures between 150 and 390 °C due to the oxidation reaction of $FeTe_2$ with oxygen to form Fe_2O_3 and TeO_2. The weight loss from the decomposition of rGO was diminished by the oxidation reaction of $FeTe_2$. The $FeTe_2$−rGO hybrid powders were estimated to contain ~5 wt % rGO from the TG analysis and elemental analysis (EA) in Figure S4 and Table S1.

An identical process was applied to prepare the bare $FeTe_2$ powders as for the $FeTe_2$−rGO hybrid powders. The spray drying of the iron nitrate aqueous solution produced an aggregated and nonspherical product due to the high hygroscopicity of iron nitrate. Therefore, the spray-drying process successfully prepared a composite powder of iron nitrate and sucrose with a spherical shape (Figure S5a). The post-treatment of the spray-dried product produced the yolk−shell structured Fe_2O_3 powders by the formation mechanism described in our previous articles.[40,41] The bare Fe_2O_3 powders had a clear core@void@shell configuration (Figure S5b). The tellurization of the Fe_2O_3 powders produced the phase-pure $FeTe_2$ powders with a spherical shape and filled structure, as shown in Figure S5c. The mean size of the bare $FeTe_2$ powders was 2.4 μm, as measured from the SEM image.

The cyclic voltammograms (CVs) of the $FeTe_2$−rGO hybrid powders are shown in Figure 4a. The sharp peak located at 0.8 V was observed in the first cathodic scan of the $FeTe_2$−rGO hybrid powders. The Na-ion storage of the $FeTe_2$ materials occurred by a conversion reaction, similar to that for transition-

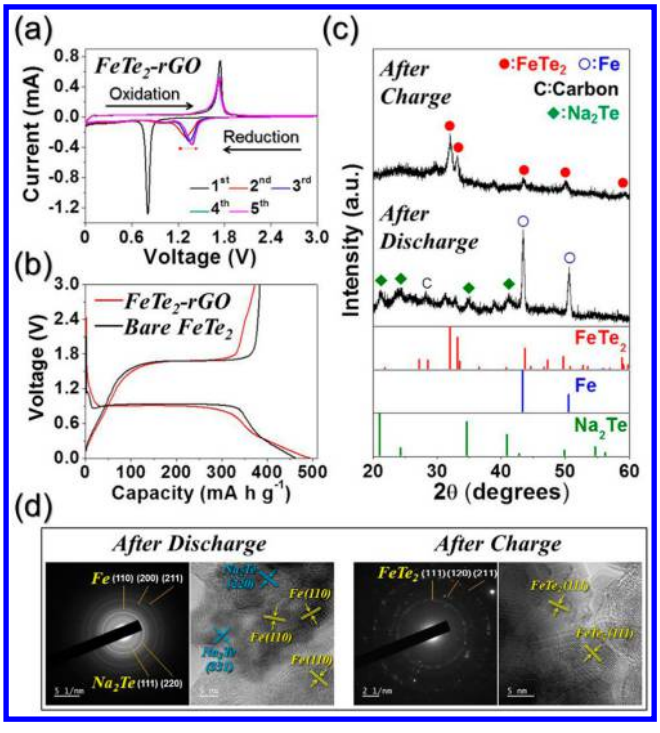

Figure 4. (a) Cyclic voltammogram curves of the $FeTe_2$-decorated rGO hybrid powders at a scan rate of 0.07 mV s^{-1}, (b) initial discharge−charge profiles of the $FeTe_2$-decorated rGO hybrid powders and bare $FeTe_2$ powders in the voltage range of 0.01−3.0 V, (c) ex situ XRD patterns of the reaction products after first fully discharged and charged process, and (d) corresponding HR-TEM images and SAED patterns.

DOI: 10.1021/acsami.6b05758
ACS Appl. Mater. Interfaces 2016, 8, 21343−21349

metal sulfide and selenide materials.[17,21,25] Therefore, the distinct reduction peak located at ~1.35 V was attributed to the formation of metallic Fe nanocrystals and Na_2Te by a conversion reaction of $FeTe_2$ with Na ions. A distinct oxidation peak (1.73 V) was observed in the anodic scans, which was attributed to the formation of $FeTe_2$. The peak location of the cathodic scans shifted to a higher potential after first cycle due to the formation of $FeTe_2$ with ultrafine nanocrystals.[42,43] The initial discharge and charge profiles of the $FeTe_2$–rGO hybrid and bare $FeTe_2$ powders at a current density of 0.2 A g^{-1} are shown in Figure 4b. The two samples had similarly shaped discharge and charge curves. The long plateaus at 0.93 and 1.68 V were observed in their first discharge and charge process, respectively. The initial discharge capacities of the $FeTe_2$–rGO hybrid and bare $FeTe_2$ powders were 493 and 462 mA h g^{-1}, respectively; their corresponding initial charge capacities were 373 and 384 mA h g^{-1}, respectively. The $FeTe_2$–rGO hybrid powders had a slightly lower initial Coulombic efficiency than the bare $FeTe_2$ powders (76% and 83%, respectively) due to the high initial irreversible capacity loss of rGO for Na-ion storage.

The electrochemical reaction mechanism of $FeTe_2$ with the sodium ions was analyzed by ex situ XRD, SAED patterns, and corresponding HR-TEM using the cell after the fully discharged and charged states at 0.05 and 3.0 V, respectively. Figure 4c shows the ex situ XRD patterns of the $FeTe_2$–rGO hybrid powder electrode at the fully discharged and charged states. After a full discharge (0.05 V), the peaks of the Na_2Te and Fe phases were observed with the conductive carbon (carbon black). The peaks of the $FeTe_2$ phase were confirmed at the fully charged state (3.0 V). The SAED patterns shown in Figure 4d also confirmed the conversion reaction process. When discharged to 0.05 V, the rings were indexed to the metallic Fe and Na_2Te phases. The rings of the $FeTe_2$ phase were observed after a full charge at 3.0 V (Figure 4d). The HR-TEM images of the fully discharged and charged $FeTe_2$–rGO hybrid powder electrode were also consistent with these above results. At a discharge of 0.05 V, the lattice fringe with a 0.208 nm *d*-space was indexed to the (110) plane of Fe. The interplanar spacings of 0.259 and 0.168 nm correspond to the (220) and (331) planes of Na_2Te, respectively. When charged to 3.0 V, the (111) planes with a 0.280 nm *d*-space of $FeTe_2$ was observed. These provided the electrochemical reaction mechanism of $FeTe_2$ for Na-ion storage, as outlined in Equations 1 and (2).

Discharge process:

$$FeTe_2 + 4Na^+ + 4e^- \rightarrow Fe + 2Na_2Te \quad (1)$$

Charge process:

$$Fe + 2Na_2Te \rightarrow FeTe_2 + 4Na^+ + 4e^- \quad (2)$$

The capacities of the $FeTe_2$–rGO hybrid powders were maintained during the first 40 cycles at a current density of 0.2 A g^{-1} and then slightly decreased during the next 40 cycles in Figure 5a. The capacities of the bare $FeTe_2$ powders dropped significantly after the first 20 cycles. The discharge capacities of the $FeTe_2$-decorated rGO hybrid powders for the first and 80th cycles were 493 and 293 mA h g^{-1}, respectively, and their corresponding volumetric capacities were 3974 and 2362 mA h cm^{-3}, respectively. The capacity retentions of the $FeTe_2$–rGO hybrid and bare $FeTe_2$ powders measured from the second cycle were 69 and 20%, respectively. Partial structural destruction of the $FeTe_2$–rGO hybrid powders during the first 20 cycles resulted in the low Coulombic efficiencies below

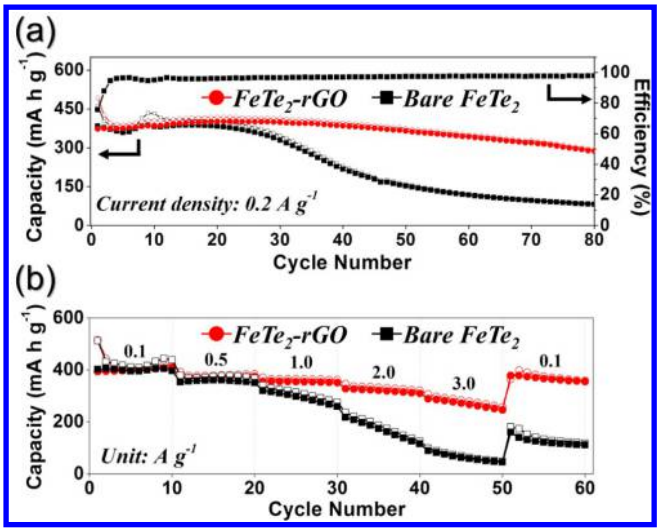

Figure 5. (a) Cycling performances at a current density of 0.2 A g^{-1} and (b) rate performances (from 0.1 to 3.0 A g^{-1}) of the $FeTe_2$-decorated rGO hybrid powders and bare $FeTe_2$ powders.

95%. However, the $FeTe_2$–rGO hybrid powders induced high Coulombic efficiencies above 98% from the 20th cycle onward. The rate performances of the two samples are shown in Figure 5b. The $FeTe_2$–rGO hybrid powders showed better rate performance than that of the bare $FeTe_2$ powders. The $FeTe_2$–rGO hybrid had final discharge capacities of 421, 384, 362, 321, and 257 mA h g^{-1} at current densities of 0.1, 0.5, 1.0, 2.0, and 3.0 A g^{-1}, respectively.

The superior Na-ion storage performance of the $FeTe_2$–rGO hybrid powders was investigated by electrochemical impedance spectroscopy (EIS) and compared to that of the bare $FeTe_2$ powders. The Nyquist plots of the $FeTe_2$ cells before and after 1, 5, 50, and 80 cycles were obtained by deconvolution with a Randle-type equivalent circuit model (Figure S6), as shown in Figure 6.[44,45] The $FeTe_2$–rGO hybrid powders with high electrical conductivity due to rGO had lower R_{ct} value of 342 Ω than that of 494 Ω for bare $FeTe_2$ powders, as shown in Figure 6a.[46−48] Figure 6b shows the relationship between Z_{re} and $\omega^{-1/2}$ in the low-frequency (f) region, where ω is the angular frequency ($\omega = 2\pi f$). The less steep slope at the low frequency indicated higher sodium ion diffusivity in the $FeTe_2$–rGO hybrid powders.[49] The ultrafine $FeTe_2$ nanocrystals provided high sodium ion diffusivity in the $FeTe_2$–rGO hybrid powders. The charge-transfer resistances of the $FeTe_2$–rGO hybrid powders before cycling and at 1, 5, 50, and 80 cycles (shown in Figure 6a,c) were 342, 59, 38, 39, and 41 Ω, respectively. The formation of ultrafine $FeTe_2$ nanocrystals during the first cycle distinctly decreased the charge-transfer resistance. In addition, the further decrease of the R_{ct} during further four cycles was attributed to the gradual activation of the $FeTe_2$–rGO hybrid powders. The R_{ct} values of the bare $FeTe_2$ powders before cycling and at 1, 5, 50, and 80 cycles shown in Figure 6a,d were 494, 119, 78, 124, and 221 Ω, respectively. The R_{ct} values of the bare $FeTe_2$ powders increased significantly after five cycles due to the structural destruction during repeated sodium ion insertion and desertion processes.

The morphological changes of the two samples obtained after 80 cycles are shown in Figure 7. The spherical bare $FeTe_2$ powder was broken into several pieces after cycling (Figure 7a). However, the overall morphology of the $FeTe_2$–rGO hybrid powders was maintained after cycling (Figure 7b). In Figure

DOI: 10.1021/acsami.6b05758
ACS Appl. Mater. Interfaces 2016, 8, 21343−21349

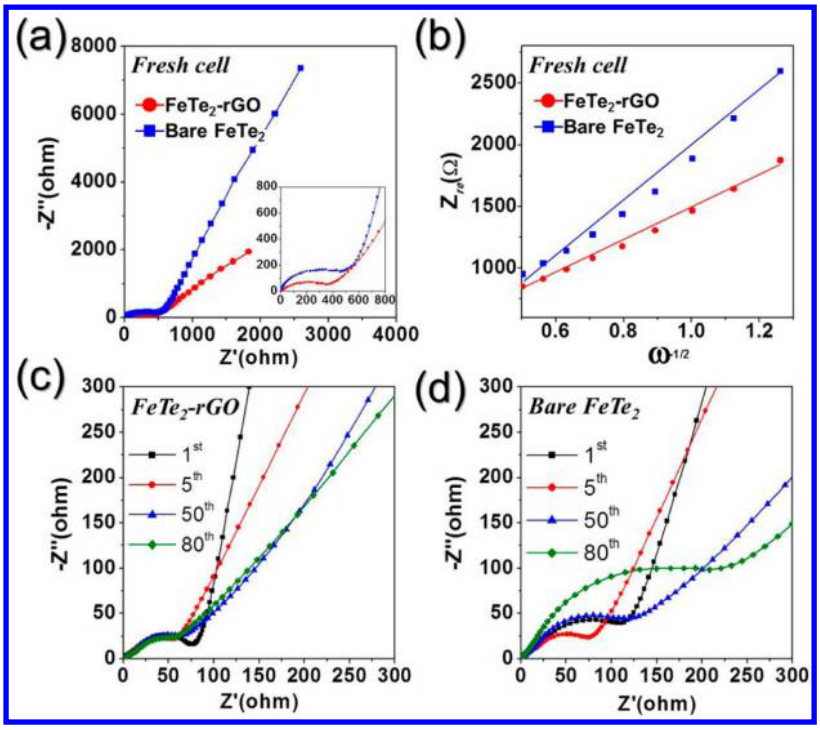

Figure 6. (a, c, d) Nyquist impedance plots and (b) relationships between the real part of the impedance (Z_{re}) and $\omega^{-1/2}$ of the $FeTe_2$-decorated rGO hybrid powders and bare $FeTe_2$ powders before and after cycling.

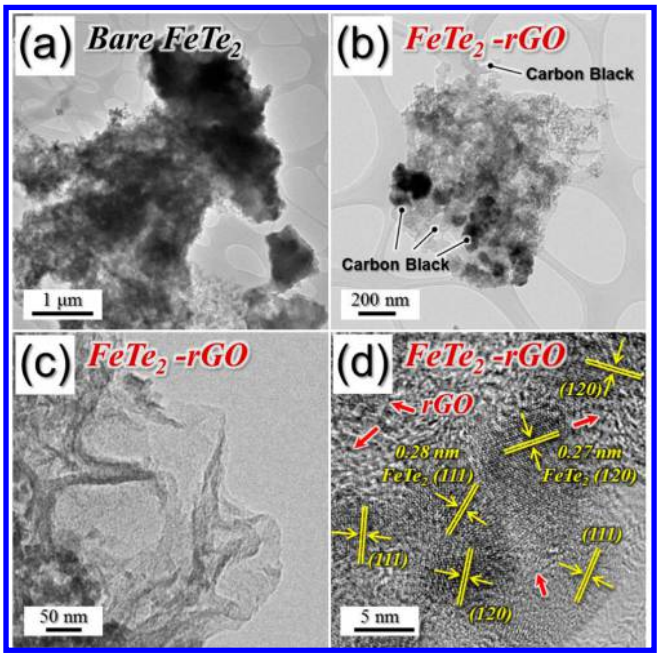

Figure 7. TEM images of (a) bare $FeTe_2$ powders and (b–d) $FeTe_2$-decorated rGO hybrid powders after 80 cycles.

7c,d, several $FeTe_2$ nanoparticles surrounded by rGO remained after cycling, indicating that the aggregation and growth of $FeTe_2$ particles were effectively avoided. An HR-TEM image (Figure 7d) showed that most primary nanoparticles had lattice spacings of 0.27 and 0.28 nm, corresponding to the (120) and (111) planes of the $FeTe_2$ phase, respectively. This result was consistent with the CV result indicating that sodium storage was highly reversible for the nanocomposites because Fe could be effectively oxidized to $FeTe_2$.

The sodium-ion storage performances of the $FeTe_2$-decorated rGO hybrid powders were compared to those of the metal chalcogenide materials reported in the literature, and the results were summarized in Table S2. Some of metal chalcogenide materials reported in the literature had higher capacities than that of the $FeTe_2$-decorated rGO hybrid powders. In this study, transition-metal telluride material was first studied as a possible electrode material of NIBs. In addition, the electrochemical reaction mechanism of $FeTe_2$ for Na-ion storage was studied. However, the optimization of the rGO content as well as the preparation conditions should be performed to enhance the sodium-ion storage performances of the $FeTe_2$-decorated rGO hybrid powders.

CONCLUSIONS

$FeTe_2$–rGO hybrid powders with a spherical-like shape and fine size were studied as anode materials for NIBs. The one-pot tellurization process of the spray pyrolysis product led to $FeTe_2$–rGO hybrid powders with good Na-ion storage. The Na-ion storage of the $FeTe_2$ material occurred by a conversion reaction. The $FeTe_2$–rGO hybrid powders with porous structures and high electrical conductivity showed superior Na-ion storage performances than those of the bare $FeTe_2$ powders. The simple process introduced in this study could be applied to the preparation of transition-metal telluride–rGO hybrid powders with various compositions and various rGO contents for wide applications, including energy storage, hydrogen evolution reactions, and oxygen reduction reactions.

ASSOCIATED CONTENT

Supporting Information

The Supporting Information is available free of charge on the ACS Publications website at DOI: 10.1021/acsami.6b05758.

DOI: 10.1021/acsami.6b05758
ACS Appl. Mater. Interfaces 2016, 8, 21343–21349

Characterization method of the materials, detailed electrochemical measurements, schematic diagram of the spray pyrolysis and pilot-scale spray drying system applied in the study, SEM images and XRD patterns of the Fe_3O_4-decorated rGO hybrid powders, TG, elemental analysis of the $FeTe_2$-decorated rGO hybrid powders, SEM images and XRD patterns of the bare $FeTe_2$ powders, Randle-type equivalent circuit model used for alternating current impedance fitting, CV curves of the bare $FeTe_2$ powders. (PDF)

AUTHOR INFORMATION

Corresponding Authors

*E-mail: yckang@korea.ac.kr. (Y.C.K.)

*E-mail: jkrhee@konkuk.ac.kr. Fax: (+82) 2-928-3584. (J.-K.L.)

Notes

The authors declare no competing financial interest.

ACKNOWLEDGMENTS

This work was supported by a National Research Foundation of Korea (NRF) grant funded by the Korea government (NRF-2015R1A2A1A15056049). This work was supported by the Energy Efficiency & Resources Core Technology Program of the Korea Institute of Energy Technology Evaluation and Planning, granted financial resource from the Ministry of Trade, Industry & Energy, Republic of Korea (201320200000420 and 20153030091450).

REFERENCES

(1) Li, W.; Yang, Z.; Li, M.; Jiang, Y.; Wei, X.; Zhong, X.; Gu, L.; Yu, Y. Amorphous Red Phosphorus Embedded in Highly Ordered Mesoporous Carbon with Superior Lithium and Sodium Storage Capacity. *Nano Lett.* **2016**, *16*, 1546−1553.

(2) Palomares, V.; Serras, P.; Villaluenga, I.; Hueso, K. B.; Carretero-González, J.; Rojo, T. Na-Ion Batteries, Recent Advances and Present Challenges to Become Low Cost Energy Storage Systems. *Energy Environ. Sci.* **2012**, *5*, 5884−5901.

(3) Qian, J.; Xiong, Y.; Cao, Y.; Ai, X.; Yang, H. Synergistic Na-Storage Reactions in Sn_4P_3 as a High-Capacity, Cycle-Stable Anode of Na-Ion Batteries. *Nano Lett.* **2014**, *14*, 1865−1869.

(4) Wang, L.; Lu, Y.; Liu, J.; Xu, M.; Cheng, J.; Zhang, D.; Goodenough, J. B. A Superior Low−Cost Cathode for a Na−Ion Battery. *Angew. Chem., Int. Ed.* **2013**, *52*, 1964−1967.

(5) Wang, S.; Xia, L.; Yu, L.; Zhang, L.; Wang, H.; Lou, X. W. D. Free−Standing Nitrogen−Doped Carbon Nanofiber Films: Integrated Electrodes for Sodium−Ion Batteries with Ultralong Cycle Life and Superior Rate Capability. *Adv. Energy Mater.* **2016**, *6*, 1502217.

(6) Dahbi, M.; Yabuuchi, N.; Kubota, K.; Tokiwa, K.; Komaba, S. Negative Electrodes for Na-Ion Batteries. *Phys. Chem. Chem. Phys.* **2014**, *16*, 15007−15028.

(7) Islam, M. S.; Fisher, C. A. J. Lithium and Sodium Battery Cathode Materials: Computational Insights Into Voltage, Diffusion and Nanostructural Properties. *Chem. Soc. Rev.* **2014**, *43*, 185−204.

(8) Slater, M. D.; Kim, D.; Lee, E.; Johnson, C. S. Sodium−Ion Batteries. *Adv. Funct. Mater.* **2013**, *23*, 947−958.

(9) Song, H.; Li, N.; Cui, H.; Wang, C. Enhanced Storage Capability and Kinetic Processes by Pores-and Hetero-Atoms-Riched Carbon Nanobubbles for Lithium-Ion and Sodium-Ion Batteries Anodes. *Nano Energy* **2014**, *4*, 81−87.

(10) Balogun, M. − S.; Luo, Y.; Lyu, F.; Wang, F.; Yang, H.; Li, H.; Liang, C.; Huang, M.; Huang, Y.; Tong, Y. Carbon Quantum Dots Surface Engineered VO_2 Interwoven Nanowires: A Flexible Cathode Material for Lithium and Sodium Ion Batteries. *ACS Appl. Mater. Interfaces* **2016**, *8*, 9733−9744.

(11) Yan, Y.; Yin, Y. X.; Guo, Y.-G.; Wan, L. J. A Sandwich−Like Hierarchically Porous Carbon/Graphene Composite as a High−Performance Anode Material for Sodium−Ion Batteries. *Adv. Energy Mater.* **2014**, *4*, 1301584.

(12) Yu, D. Y. W.; Prikhodchenko, P. V.; Mason, C. W.; Batabyal, S. K.; Gun, J.; Sladkevich, S.; Medvedev, A. G.; Lev, O. High-Capacity Antimony Sulphide Nanoparticle-Decorated Graphene Composite as Anode for Sodium-Ion Batteries. *Nat. Commun.* **2013**, *4*, 2922.

(13) Hu, Z.; Wang, L.; Zhang, K.; Wang, J.; Cheng, F.; Tao, Z.; Chen, J. MoS_2 Nanoflowers with Expanded Interlayers as High−Performance Anodes for Sodium−Ion Batteries. *Angew. Chem.* **2014**, *126*, 13008−13012.

(14) Kim, Y.; Kim, Y.; Park, Y.; Jo, Y. N.; Kim, Y.-J.; Choi, N.-S.; Lee, K. T. SnSe Alloy as a Promising Anode Material for Na-Ion Batteries. *Chem. Commun.* **2015**, *51*, 50−53.

(15) Saha, P.; Jampani, P. H.; Datta, M. K.; Hong, D.; Okoli, C. U.; Manivannan, A.; Kumta, P. N. Electrochemical Performance of Chemically and Solid State-Derived Chevrel Phase Mo_6T_8 (T= S, Se) Positive Electrodes for Sodium-Ion Batteries. *J. Phys. Chem. C* **2015**, *119*, 5771−5782.

(16) Yu, X. Y.; Yu, L.; Lou, X. W. D. Metal Sulfide Hollow Nanostructures for Electrochemical Energy Storage. *Adv. Energy Mater.* **2016**, *6*, 1501333.

(17) Zhang, K.; Hu, Z.; Liu, X.; Tao, Z.; Chen, J. $FeSe_2$ Microspheres as a High−Performance Anode Material for Na−Ion Batteries. *Adv. Mater.* **2015**, *27*, 3305−3309.

(18) Cummins, D. R.; Russell, H. B.; Jasinski, J. B.; Menon, M.; Sunkara, M. K. Iron Sulfide (FeS) Nanotubes using Sulfurization of Hematite Nanowires. *Nano Lett.* **2013**, *13*, 2423−2430.

(19) Dagotto, E. Colloquium: The Unexpected Properties of Alkali Metal Iron Selenide Superconductors. *Rev. Mod. Phys.* **2013**, *85*, 849−867.

(20) Di Giovanni, C.; Wang, W.-A.; Nowak, S.; Grenèche, J.-M.; Lecoq, H.; Mouton, L.; Giraud, M.; Tard, C. Bioinspired Iron Sulfide Nanoparticles for Cheap and Long-Lived Electrocatalytic Molecular Hydrogen Evolution in Neutral Water. *ACS Catal.* **2014**, *4*, 681−687.

(21) Kim, T. B.; Choi, J. W.; Ryu, H. S.; Cho, G. B.; Kim, K. W.; Ahn, J. H.; Cho, K. K.; Ahn, H. J. Electrochemical Properties of Sodium/Pyrite Battery at Room Temperature. *J. Power Sources* **2007**, *174*, 1275−1278.

(22) Liu, J.; Tang, Q.; He, B.; Yu, L. Cost-Effective, Transparent Iron Selenide Nanoporous Alloy Counter Electrode for Bifacial Dye-Sensitized Solar Cell. *J. Power Sources* **2015**, *282*, 79−86.

(23) Sedlmaier, S. J.; Cassidy, S. J.; Morris, R. G.; Drakopoulos, M.; Reinhard, C.; Moorhouse, S. J.; O'Hare, D.; Manuel, P.; Khalyavin, D.; Clarke, S. J. Ammonia-Rich High-Temperature Superconducting Intercalates of Iron Selenide Revealed through Time-Resolved in Situ X-Ray and Neutron Diffraction. *J. Am. Chem. Soc.* **2014**, *136*, 630−633.

(24) Wang, Y.-X.; Yang, J.; Chou, S.-L.; Liu, H. K.; Zhang, W.-x.; Zhao, D.; Dou, S. X. Uniform Yolk-Shell Iron Sulfide-Carbon Nanospheres for Superior Sodium-Iron Sulfide Batteries. *Nat. Commun.* **2015**, *6*, 8689.

(25) Park, G. D.; Cho, J. S.; Lee, J.-K.; Kang, Y. C. Na-Ion Storage Performances of $FeSe_x$ and Fe_2O_3 Hollow Nanoparticles-Decorated Reduced Graphene Oxide Balls Prepared by Nanoscale Kirkendall Diffusion Process. *Sci. Rep.* **2016**, *6*, 22432.

(26) Han, Y.; Li, W. Y.; Cao, L. X.; Wang, X. Y.; Xu, B.; Zhao, B. R.; Guo, Y. Q.; Yang, J. L. Superconductivity in Iron Telluride Thin Films under Tensile Stress. *Phys. Rev. Lett.* **2010**, *104*, 017003.

(27) Nie, Y. F.; Telesca, D.; Budnick, J. I.; Sinkovic, B.; Wells, B. O. Superconductivity Induced in Iron Telluride Films by Low-Temperature Oxygen Incorporation. *Phys. Rev. B: Condens. Matter Mater. Phys.* **2010**, *82*, 020508.

(28) Turner, A. M.; Wang, F.; Vishwanath, A. Kinetic Magnetism and Orbital Order in Iron Telluride. *Phys. Rev. B: Condens. Matter Mater. Phys.* **2009**, *80*, 224504.

(29) Liu, J.; Wu, C.; Xiao, D.; Kopold, P.; Gu, L.; van Aken, P. A.; Maier, J.; Yu, Y. MOF-Derived Hollow Co_9S_8 Nanoparticles

DOI: 10.1021/acsami.6b05758
ACS Appl. Mater. Interfaces 2016, 8, 21343−21349

Embedded in Graphitic Carbon Nanocages with Superior Li-Ion Storage. *Small* **2016**, *12*, 2354−2364.
(30) Wang, X.; Li, G.; Hassan, F. M.; Li, J.; Fan, X.; Batmaz, R.; Xiao, X.; Chen, Z. W. Sulfur Covalently Bonded Graphene with Large Capacity and High Rate for High-Performance Sodium-ion Batteries Anodes. *Nano Energy* **2015**, *15*, 746−754.
(31) Xu, M.; Liang, T.; Shi, M.; Chen, H. Graphene-Like Two-Dimensional Materials. *Chem. Rev.* **2013**, *113*, 3766−3798.
(32) Wang, Y.; Qian, B.; Li, H.; Liu, L.; Chen, L.; Jiang, H. VSe_2/Graphene Nanocomposites as Anode Materials for Lithium-Ion Batteries. *Mater. Lett.* **2015**, *141*, 35−38.
(33) Xue, D.-J.; Xin, S.; Yan, Y.; Jiang, K.-C.; Yin, Y.-X.; Guo, Y.-G.; Wan, L.-J. Improving the Electrode Performance of Ge through Ge@C Core−Shell Nanoparticles and Graphene Networks. *J. Am. Chem. Soc.* **2012**, *134*, 2512−2515.
(34) Park, G. D.; Cho, J. S.; Kang, Y. C. Sodium-Ion Storage Properties of Nickel Sulfide Hollow Nanospheres/Reduced Graphene Oxide Composite Powders Prepared by a Spray Drying Process and the Nanoscale Kirkendall Effect. *Nanoscale* **2015**, *7*, 16781−16788.
(35) Cho, J. S.; Lee, S. Y.; Kang, Y. C. First Introduction of $NiSe_2$ to Anode Material for Sodium-Ion Batteries: A Hybrid of Graphene-Wrapped $NiSe_2$/C Porous Nanofiber. *Sci. Rep.* **2016**, *6*, 23338.
(36) Ferrari, A. C.; Meyer, J. C.; Scardaci, V.; Casiraghi, C.; Lazzeri, M.; Mauri, F.; Piscanec, S.; Jiang, D.; Novoselov, K. S.; Roth, S.; et al. Raman Spectrum of Graphene and Graphene Layers. *Phys. Rev. Lett.* **2006**, *97*, 187401.
(37) Telesca, D.; Nie, Y.; Budnick, J. I.; Wells, B. O.; Sinkovic, B. Impact of Valence States on the Superconductivity of Iron Telluride and Iron Selenide Films with Incorporated Oxygen. *Phys. Rev. B: Condens. Matter Mater. Phys.* **2012**, *85*, 214517.
(38) Park, G. D.; Cho, J. S.; Kang, Y. C. Novel Cobalt Oxide-Nanobubble-Decorated Reduced Graphene Oxide Sphere with Superior Electrochemical Properties Prepared by Nanoscale Kirkendall Diffusion Process. *Nano Energy* **2015**, *17*, 17−26.
(39) Monson, P. A. Understanding Adsorption/Desorption Hysteresis for Fluids in Mesoporous Materials using Simple Molecular Models and Classical Density Functional Theory. *Microporous Mesoporous Mater.* **2012**, *160*, 47−66.
(40) Hong, Y. J.; Son, M. Y.; Kang, Y. C. One−Pot Facile Synthesis of Double−Shelled SnO_2 Yolk−Shell−Structured Powders by Continuous Process as Anode Materials for Li−Ion Batteries. *Adv. Mater.* **2013**, *25*, 2279−2283.
(41) Son, M. Y.; Hong, Y. J.; Lee, J.-K.; Chan Kang, Y. One-Pot Synthesis of Fe_2O_3 Yolk−Shell Particles with Two, Three, and Four Shells for Application as an Anode Material in Lithium-Ion Batteries. *Nanoscale* **2013**, *5*, 11592−11597.
(42) Cho, J. S.; Won, J. M.; Lee, J.-H.; Kang, Y. C. Synthesis and Electrochemical Properties of Spherical and Hollow-Structured NiO Aggregates Created by Combining the Kirkendall Effect and Ostwald Ripening. *Nanoscale* **2015**, *7*, 19620−19626.
(43) Sun, Y.; Hu, X.; Luo, W.; Xia, F.; Huang, Y. Reconstruction of Conformal Nanoscale MnO on Graphene as a High−Capacity and Long−Life Anode Material for Lithium Ion Batteries. *Adv. Funct. Mater.* **2013**, *23*, 2436−2444.
(44) Wu, H.; Xu, M.; Wang, Y.; Zheng, G. Branched Co_3O_4/Fe_2O_3 Nanowires as High Capacity Lithium-Ion Battery Anodes. *Nano Res.* **2013**, *6*, 167−173.
(45) Wu, H.; Xu, M.; Wu, H.; Xu, J.; Wang, Y.; Peng, Z.; Zheng, G. Aligned NiO Nanoflake Arrays Grown on Copper as High Capacity Lithium-Ion Battery Anodes. *J. Mater. Chem.* **2012**, *22*, 19821−19825.
(46) Cho, J. S.; Hong, Y. J.; Kang, Y. C. Design and Synthesis of Bubble-Nanorod-Structured Fe_2O_3−Carbon Nanofibers as Advanced Anode Material for Li-Ion Batteries. *ACS Nano* **2015**, *9*, 4026−4035.
(47) Wang, Z.; Luan, D.; Madhavi, S.; Hu, Y.; Lou, X. W. D. Assembling Carbon-Coated α-Fe_2O_3 Hollow Nanohorns on the CNT Backbone for Superior Lithium Storage Capability. *Energy Environ. Sci.* **2012**, *5*, 5252−5256.
(48) Xu, Y.; Zhu, Y.; Liu, Y.; Wang, C. Electrochemical Performance of Porous Carbon/Tin Composite Anodes for Sodium−Ion and Lithium−Ion Batteries. *Adv. Energy Mater.* **2013**, *3*, 128−133.
(49) Liu, G. Q.; Kuo, H. T.; Liu, R. S.; Shen, C. H.; Shy, D. S.; Xing, X. K.; Chen, J. M. Study of Electrochemical Properties of Coating ZrO_2 on $LiCoO_2$. *J. Alloys Compd.* **2010**, *496*, 512−516.

DOI: 10.1021/acsami.6b05758
ACS Appl. Mater. Interfaces 2016, 8, 21343−21349